Surface Characterization Methods—
XPS, TOF-SIMS, and SAM
A Complimentary Ensemble of Tools

J.E. deVries

X-ray photoelectron spectroscopy (XPS), time-of-flight secondary ion mass spectrometry (TOF-SIMS), and scanning auger microscopy (SAM) analytical techniques have played important roles in the characterization of the surface and the interfacial chemistry governing properties and performance of materials, and material interfaces. These techniques afford spatially resolved elemental and molecular analysis of the topmost atomic layers of solid surfaces and interfaces. Currently available instrumentation provides qualitative/quantitative analysis on molecularly complex materials with detection limits in the parts-per-billion (ppb) range and spatial resolutions approaching 30 nm. Each technique is unique in the information attained, therefore necessitating a multitechnique approach to achieve a complete surface characterization. Examples of coating/interfacial characterization by XPS, TOF-SIMS, and SAM are presented illustrating the functionality of these tools and the complimentary natures of them.

Keywords   coating characterization, failure analysis

---

1. Introduction

In the past 20 years, surface analytical techniques have evolved into powerful tools as applied to the characterization of materials, coatings, and interfaces. These techniques not only determine the chemical composition, molecular orientation, and physical structure of the first few layers of atoms, but may also include similar information to depths of several microns. Such information enables academic and industrial research groups to understand basic chemical and physical processes that affect material or device performance. X-ray photoelectron spectroscopy (XPS), secondary ion mass spectrometry (SIMS), and scanning auger microscopy (SAM) are commonly used surface analytical tools when applied to material and interface characterization.

Scanning auger microscopy is based on a more generic surface analytical technique known as Auger electron spectroscopy (AES) (Ref 1, 2). This technique provides both elemental and limited chemical bonding information for all elements of the periodic table except hydrogen and helium. Materials that are either conductive or insulative can be characterized; however, analyses of insulating materials may sometimes be difficult. The probe depth of SAM is 0.5 to 5 nm, making the technique extremely surface sensitive. The quantitative accuracy of SAM is ±15%, and the detection limit varies from approximately 0.1 to 1.0 at.%. In methodologies similar to scanning electron microscopy (SEM), the raster of a primary electron beam is synchronized with the electrons, which are energy filtered and subsequently detected. Spatial resolutions down to 30 nm can be obtained from commercially available instruments. Elemental images or maps of surfaces can be routinely acquired, as well as spatially resolved line scans across the sample surface. The secondary, non-Auger electrons can also be detected to produce higher quality images comparable to SEM micrographs. To attain deeper, near surface information, the SAM process is combined with depth profiling by sputtering the surface with inert gas ions. This process physically erodes the surface to expose underlying layers and chemistries for subsequent Auger analysis.

X-ray photoelectron spectroscopy, also known as electron spectroscopy for chemical analysis (ESCA), is a widely used technique for investigating the chemistry of solid surfaces (Ref 1, 2). The technique provides both elemental and chemical state information for all elements of the periodic table except helium and hydrogen. Materials that are either conductive or insulating can be accommodated. The probe depth of XPS is only ~3 nm, again making this technique extremely surface sensitive. The accuracy of XPS is approximately ±10%, and the detection limit varies from ~0.1 to 1.0 at.%. The spatial resolution of this technique has been continually improving over recent years either by controlling a variable spot x-ray source or by aperaturing the area imaged by the analyzer. Spatial resolutions <50 µm can easily be attained. The acquisition of line scans and maps are also achieved through sequential multiple-point analyses. Shallow from 1.5 to 10 nm, nondestructive depth profiling, commonly referred to as angle-resolved XPS, can be accomplished by varying the photoelectron take-off angle to the detector; the probe depth varies as a function of the take-off angle. In addition, to attain information to a greater depth, XPS can be combined with ion sputtering to provide depth profiles of the near surface region. Depth profiling can be accomplished in a reasonable time frame for depths up to ~300 nm.

Time-of-flight secondary ion mass spectrometry is also based on a more generic technique, secondary ion mass spectrometry (SIMS) (Ref 3). The SIMS technique uses an ion sputtering process to actually remove material from the surface to

J.E. deVries, Ford Motor Company, Scientific Research Laboratory, MD 3061, 20000 Rotunda, Dearborn, MI 48121-2053.

---

be analyzed, therefore making this technique destructive to the original surface. The current density of the primary ion beam dictates the erosion rate of the sample material. At low current densities (static SIMS) less than a monolayer per hour is removed, making this the most surface sensitive of the techniques described. At higher rates (dynamic SIMS), microns of material may be sputtered off the surface. Materials that are either conductive or insulating can be characterized; however, analyses of insulating materials may be difficult sometimes. Both monoatomic (elemental) and polyatomic (molecular) ions are produced and are analyzed by common mass spectrometric techniques. The mass resolution and mass accuracy of these techniques afford molecular specific information to be obtained. When this technique is used in the dynamic mode, depth information to many microns can be obtained by simply analyzing and monitoring the ions removed as a function of time. The sensitivity of this technique is varied, dependent on the composition of the sample analyzed. Detection limits within the parts-per-billion (ppb) range can be obtained on some materials. The sample dependent sensitivity, however, makes quantification difficult; therefore, SIMS techniques are not as reliable, quantitatively, as the prior techniques. Spatial information in the form of images, maps, and line scans are in either a microscope or microprobe mode. The ultimate spatial resolution attainable is 100 nm. TOF-SIMS denotes that a time-of-flight mass spectrometer is used to analyze the sputtered material, serving to enhance the molecular information attainable.

Each of these techniques requires ultra-high vacuum (UHV), at least below 10^{-6} Pa, for instrument operation, restricting analyses to solid materials with low vapor pressures. Characterization of materials with a higher vapor pressure can be accommodated by analyses at subambient temperatures. An overall comparison of the capabilities of these techniques is shown in Table 1. The techniques discussed compliment each other. Demonstration of the complimentary nature of these techniques as applied to material characterization is shown. Examples of applied research programs undertaken utilizing XPS, SAM, and TOF-SIMS are given.

2. Experimental

2.1 Theory of SAM

In the AES technique, surfaces are bombarded with electrons (typically at 3 to 10 keV and a few nanoamperes), and the emitted electrons are energy analyzed and counted. Most of the emitted electrons are secondary electrons that carry no direct chemical or elemental information about the atoms that compose the sample. A small fraction of the emitted electrons are Auger electrons, that is, electrons whose energies are characteristic of the surface atoms from which they were emitted. Essentially, when a vacancy is formed in one of the inner electron shells of an atom by the emission of a secondary electron, it may be filled by either a radiative (x-ray) or nonradiative process (Auger). The nonradiative process is named after Pierre Auger, the discoverer of this phenomena. The Auger process is based on an electron from a less tightly bound orbital filling the vacancy produced by the emission of the secondary electron and a second electron (the Auger electron) being emitted into the continuum with an energy equal to the difference in the initial and final states. An example is the KLL transition shown in Fig. 1. The initial state has a hole in the K shell, and the final state has two vacancies in the L shell. Symbolically, the Auger process is represented by naming the orbitals or shells in which the vacancies occur, both in the initial and final states, as in this case a KLL transition. Auger electrons from a given element result in a unique set of peaks in an energy spectrum. This allows simple qualitative analysis of as little as 0.002 monolayer. The transition of AES to SAM results from the fact that SAM utilizes a finely focused primary electron beam rastered across the sample surface to provide spatial and chemical information as a function of primary beam position.

2.2 SAM Instrumentation

The SAM system used was a model 660 scanning auger microprobe (Perkin-Elmer, Physical Electronics, Eden Prairie, MN). The computer system used to acquire and process the data was also supplied by Perkin-Elmer, Physical Electronics. The electron optical column of the system consists of a single stage cylindrical-mirror electron energy analyzer (CMA) set at 0.6% energy resolution and an integral coaxially mounted electron gun. Spectral data were collected and stored in the E·N(E) format and were 5-point differentiated and smoothed by the Savitzky & Golay method employed in the system software. The electron beam energy used was 10 keV. The incidence angle of the electron beam to the sample normal was 30°. The diameter of the electron beam was 0.6 μm. The spectra were acquired from an area of 0.25×0.25 mm^2. Electron beam current in the range of 100 to 250 nA was measured by the system software using a +90 V bias. Depth profiling was accomplished using a duoplasmatron source microbeam ion gun with Ar$^+$ as

Table 1 Comparison of XPS, SAM, and SIMS analytical capabilities

	Static SIMS	Dynamic SIMS	XPS	SAM
Probe	Ion beam	Ion beam	X-rays	Electrons
Species detected	Ions	Ions	Electrons	Electron
Analysis depth	Monolayer	Microns	15-70 Å	15-70 Å
Surface damage	No	Yes	No	No/yes
Detection limits	10 ppm	<1 ppm	0.1 at.%	0.1 at.%
Spatial resolution	<0.1 μm	<0.1 μm	<50 μm	<0.05 μm
Elemental information	All	All	>helium	>helium
Quantification	Difficult	Difficult	Good	Good
Molecular information	Excellent	Fair	Chemical state	Chemical state

the gas ion source. An ion beam with a diameter of ~15 μm rastered an area of 0.5×0.5 mm^2 with an incidence angle of 55° to the sample normal. The ion beam current was measured with a picoammeter using +90 V bias with respect to the ground. The ion beam energy used was 2 keV, and ion beam current was 160 nA. The sputter rate for Ta_2O_5 under the same conditions was ~80 Å/min.

2.3 Theory of XPS

X-ray photoelectron spectroscopy is accomplished by irradiating a sample surface with monoenergetic soft x-rays and energy analyzing the photoelectrons emitted. Aluminum Kα x-rays (1486.6 eV) or magnesium Kα x-rays (1253.6 eV) are commonly used sources of radiation. These photons penetrate from 1 to 10 μm into a solid and interact with atoms in the surface region by the photoelectric effect, causing electrons to be emitted. Since the mean-free paths of the electrons emitted are very small, the detected electrons originate from only the top few atomic layers (0.5 to 5 nm). The emitted electrons have kinetic energies given by: $KE = hv - BE - W$, where hv is the energy of the photon, BE is the binding energy of the atomic orbital from which the electron originates, and W is the spectrometer work function. The electrons leaving the sample are detected by an electron spectrometer according to their kinetic energy. The binding energy may be regarded as an ionization energy of the atom for the particular shell involved. Since there is a variety of occupied energy levels for each type of atom, there is a corresponding variety of kinetic energies of the emitted electrons. Moreover, there is a different probability, or cross section, for each process. The energy position and intensity distribution of the photoelectron lines can be used as a fingerprint to identify the elements present, and together with measured peak areas and well-defined cross sections, quantification of the surface composition is relatively straightforward. In addition, the core-level binding energies of a certain element may change depending on the chemical state (i.e., oxidation state, lattice sites, and molecular environments) of the atom. This effect, referred to as chemical shift, is of invaluable importance for the identification of oxidation state or molecular environment of surface atoms. The XPS process is shown in Fig. 2.

2.4 XPS Instrumentation

X-ray photoelectron spectroscopy was performed with a Kratos AXIS 165 electron spectrometer (manufactured by Kratos Analytical, Manchester, England). The base pressure of the spectrometer analyzer was below 10^{-7} Pa. Photoelectrons were generated using a monochromatic Al Kα (1486.6 eV) x-ray excitation source operated at 15 kV, 20 mA (300 W) and collected using hybrid mode magnification with the analyzer at a 20 eV pass energy for high resolution spectra and a 80 eV pass energy for elemental surveys. Magnesium/aluminum atomic ratios were determined by measuring the areas generated under the spectral envelopes of the Mg $2p$ and Al $2p$ core levels collected at the 20 eV pass energy. Binding energies were referenced to the aliphatic C $1s$ line at 284.6 eV.

2.5 Theory of TOF-SIMS

The generic SIMS process is based on the impingement of an energetic primary ion beam on a material surface that sputters from the surface. Primary beam species used in SIMS include Cs^+, O_2^+, O^-, Ar^+, and Ga^+ at energies nominally between 1 and 30 keV. Sputter rates in typical SIMS experiments vary between 0.5 and 5 nm/s. Sputtering produces a host of effects including emission of secondary monatomic and polyatomic particles, resputtered primary ions, electrons, and photons from the surface. The secondary particles that are of interest carry negative, positive, and neutral charges and have kinetic energies that range from zero to several hundred electron
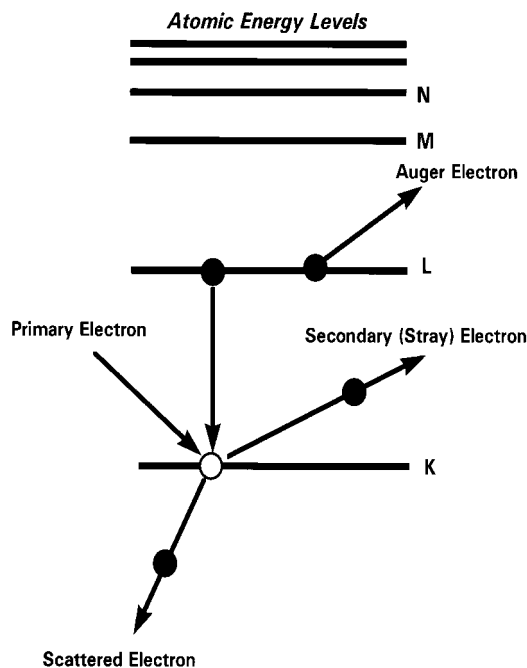

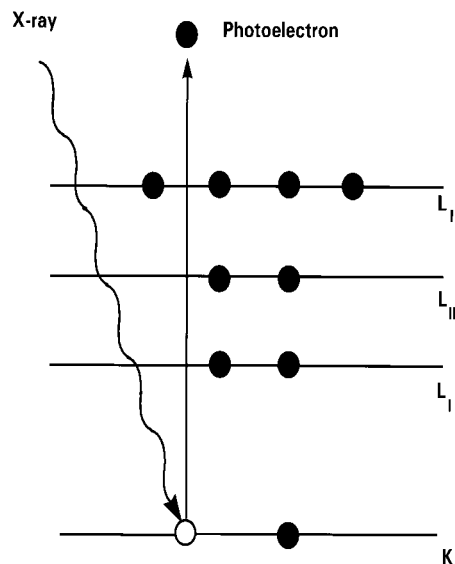
Fig. 1 Schematic of the Auger process

Fig. 2 The XPS process

volts. Figure 3 summarizes this process. Secondary ions formed in this sputtering process are extracted from the sample and analyzed via conventional mass spectrometric techniques. Mass spectra similar to those acquired in conventional mass spectrometry sample the secondary ions by continuously monitoring the ion signal, while scanning a range of mass-to-charge (m/z) ratios. The mass analyzer can be either a magnetic sector or a quadrupole system. Sputtering produces atomic ions as well as molecular ions containing more than one atom. Ion images show secondary ion intensities as a function of location on sample surfaces. Images can be acquired in either a microscope or a microprobe imaging mode. In the microprobe mode, a finely focused primary ion beam rasters the sample, and secondary ion intensity information is acquired as a function of beam position. For microscope imaging, the lateral distribution of the ions is preserved through the spectrometer so that the mass resolved image of the secondary ions can be projected onto image detectors. Monitoring the secondary ion count rate of selected elements as a function of time leads to depth profiles. The depth resolution of the experiment is therefore dependent on the sputter rate.

2.6 TOF-SIMS Instrumentation

The SIMS analyses in this study were performed using a model TFS-2000 time-of-flight SIMS instrument (manufac-
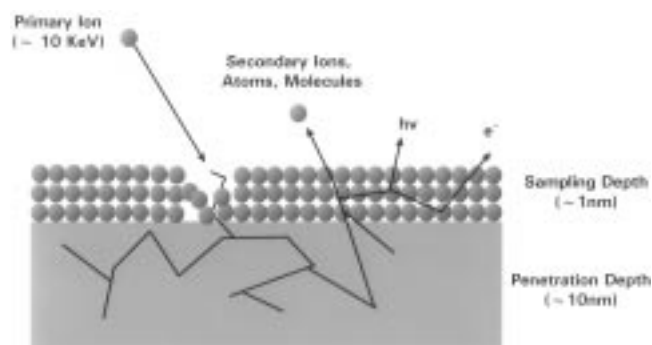

Fig. 3   Secondary ion mass spectrometry sputtering process
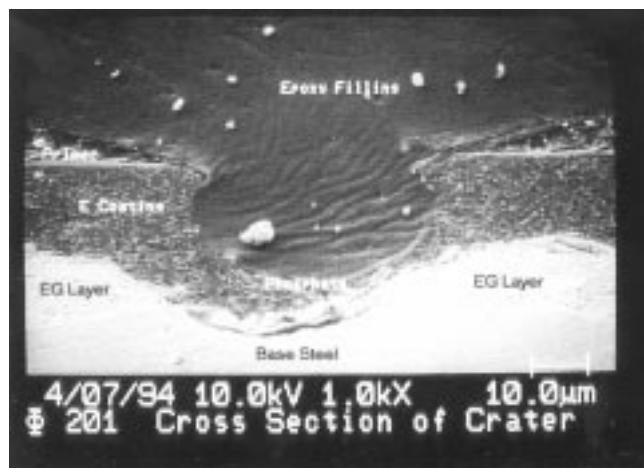

Fig. 4   Scanning auger microscopy generated SEM cross-sectional micrograph of the crater imperfection observed on an automotive paint sample

tured by Charles Evans & Associates, Redwood City, CA). This instrument uses a microfocused pulsed gallium primary ion beam rastered over the analysis area, typically 180 μm square, at 256×256 pixels resolution. The mass, position, and intensity of each secondary ion was recorded at each pixel to provide both mass and spatial information along with the intensity of each species. The distribution of chemical species can be defined within 1 μm spatial resolution, and the mass is defined within two milliatomic mass (mamu) units, or better.

3. Results and Discussion

3.1 Example 1—A Paint Defect

The final appearance of automotive paint finishes are sometimes affected by on-line manufacturing defects (e.g., cratering). Many, if not most, of these defects are associated with adventitious contamination, which falls on the wet paint prior to cure or is associated with surfaces that are not thoroughly cleaned prior to painting. This first example describes application of SAM and TOF-SIMS characterization methods to determine the cause of cratering observed in an automotive paint finish.

Modern automotive paint systems are complex, usually multilayer coating systems, where each layer serves a specific purpose. Typically, a crystalline layer of metal phosphate is first applied to bare or electrogalvanized steel prior to paint application. This layer is designed to provide increased corrosion protection for the steel. Secondly, an epoxy/urethane coating containing additional corrosion inhibitors is electrodeposited (e-coat) over the phosphate crystal surface and cured. The e-coat is then coated with a pigmented primer to improve the adhesion of subsequent coating layers and to shield the e-coat from the harmful effects of sunlight. Finally, a basecoat providing color, and a clearcoat providing gloss, are applied on the primer. Crater imperfections were observed in this example after the primer application and prior to basecoat application.

The imperfection studied in this example is clearly seen in the cross-sectional SEM micrograph given in Fig. 4, which was acquired on the SAM instrument. This micrograph clearly shows the primer, e-coat, phosphate, and electrogalvanized (EG) layers on the bare steel. The defect appears to contain no primer and a thin layer of e-coat. A definite disruption of the EG layer is also observed below the actual flaw in the organic coating. Most notable in this micrograph is the spherical character of the defect area within the electrocoat primer layer. The spherical flaws in the electrocoat were also observed in cross-sectional views of areas where there was no visible surface defect. These subsurface flaws were 10 to $20 \times$ more frequent than those visible on the top surface. In each case, the flaws are spherical and associated with a break in the EG layer in the metal substrate below. The spherical shape of the flaw indicated that a gas evolution process was occurring within the painted metal system in the bake oven during the time the electrocoat material was fluid and before electrocoat gelling/crosslinking (Ref 4) when the coating would have become solid.

The identical cross-sectional sample was analyzed by TOF-SIMS. Figures 5(a-c) represent the elemental images of this sample for iron, zinc, and carbon, respectively. The position

and morphology of the steel substrate is seen in the iron image (Fig. 5a). Superimposition of this image and the zinc image, Fig. 4b, reveals a slight depression in the steel at the sight of the defect. The bright thinner line in the zinc image can be attributed to the phosphate layer, whereas the less intense, thicker layer is the EG layer. From the zinc image, a definite break or thinning of the EG layer is also observed. Using this depression as a point of reference on the iron image (Fig. 5a), an area of lesser intensity is seen at the bottom of the depression, beneath an area of greater iron intensity. The area of lesser intensity directly corresponds to an area of greater carbon intensity as seen in Fig. 5(c). Spectral analyses of the carbon in this area reveals that it is primarily organic.

The origin of the carbon is not known but could result from two sources: adventitious contamination from processing of the substrate prior to phosphating, or intrinsic contamination originating from materials within the steel itself. In either case, the cleaning procedures utilized prior to the phosphate bath did not remove this contamination.

The paint, phosphate, and EG were removed from the bare steel to expose where the defect occurred. The SAM top surface analyses of these areas were then undertaken; the correspond-
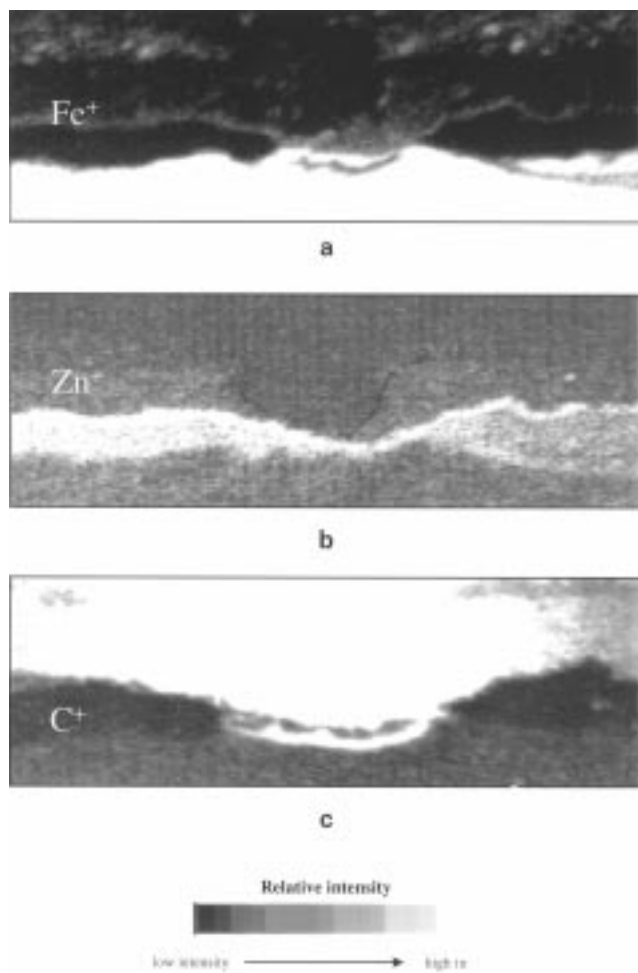
ing SAM generated SEM micrographs are given in Fig. 6. At low magnification (Fig. 6a), many scratches were observed on the surface of the bare steel. At higher magnification, the images (Fig. 6b, c) revealed a void type morphology within the scratches not normally associated with the steel substrate. In
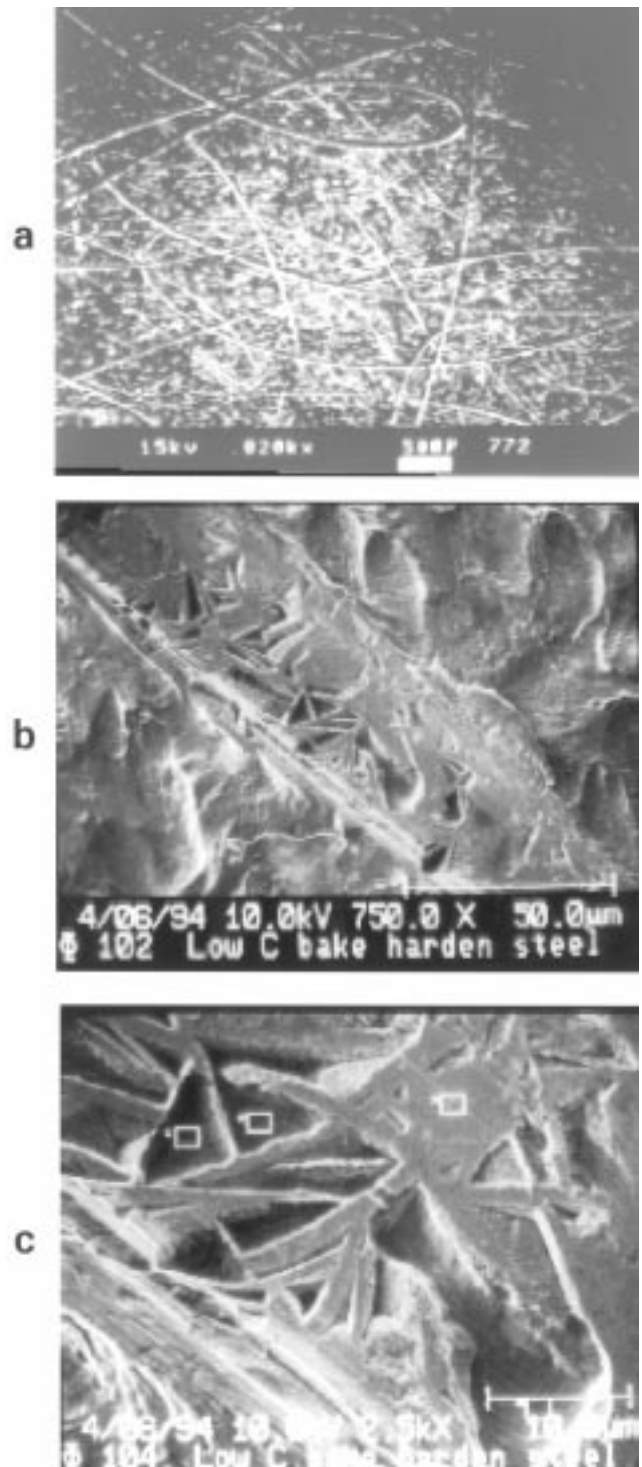

Fig. 5 Time-of-flight/secondary ion mass cross-sectional elemental ion image of the crater imperfection observed on an automotive paint sample (a) Fe^+, (b) Zn^+, and (c) C^+

Fig. 6 Scanning auger microscopy generated SEM micrographs of an area under a defect after the paint, phosphate, and EG have been removed. (a) 20×. (b) 500×. (c) 2500×. (Art has been reduced to 80% of its original size for printing.)

each case, a defect (crater) in the paint corresponded to a void structure within a scratch. Subsequent elemental analysis of the void areas and areas outside the scratch utilizing the SAM instrument are given in Table 2. This analysis reveals a much greater amount of carbon in the void areas of the scratch as compared to those areas outside the scratch, confirming the results previously described for Fig. 5. Subsequent analysis of areas within a scratch that did not exhibit the void structure revealed a composition similar to that outside the scratch. Constituents of the e-coat formulation (e.g., titanium and nitrogen) were not observed in the void area negating the possibility of e-coat residue as the source of the observed carbon. High resolution Auger line shape analysis of the carbon KLL peak revealed that the carbon was neither graphitic nor carbidic (Ref 5); it therefore was assumed to be organic, confirming TOF-SIMS spectral analyses. Sputter depth profiling of the void area revealed that the carbon observed is at least 200 nm thick, thereby verifying that it is not an adventitious result of sample handling. In all likelihood, the organic material is a source for gas volatilizing during the high bake temperatures associated with the process, which generated the spherical voids and subsequently the crater imperfections in the electrocoat primer during cure.

3.2 Example 2—Braze Alloys

To understand the dependence of aluminum alloy surface composition on aluminum braze system performance, XPS and TOF-SIMS were employed to investigate the surface composition of clad aluminum alloys. An aluminum alloy coated with a clad of aluminum and silicon was used. (Silicon was used to re-

Table 2 SAM elemental analysis of areas under a defect after the paint, phosphate, and EG have been removed

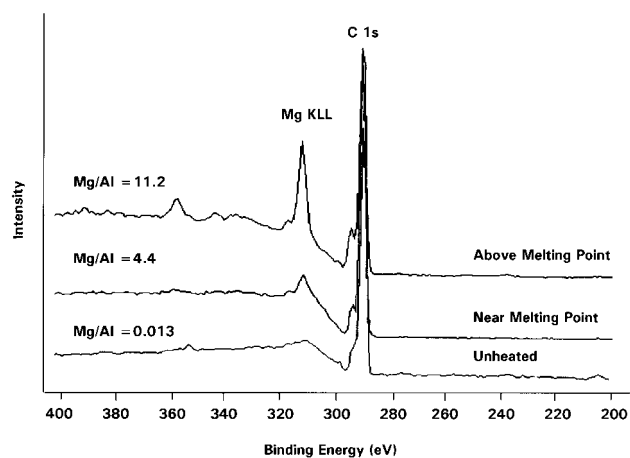| Area | Composition, % | | | | | | | | C/Fe |
	C	O	Fe	N	Ni	Cu	Zn	Other	
Inside scratch	89	5.2	4.3	2.0	…	…	…	…	20.6
Outside scratch	38	27	25	1.2	1.5	1.3	3.3	2.5	1.54

Fig. 7 X-ray photoelectron spectroscopy spectra of aluminum alloy acquired prior to heating at the clad melting point and at the clad flow temperature

duce the melting point below that of the aluminum alloy.) It is known that alloy constituents, such as magnesium, may be deleterious to the final braze performance and corrosion resistance of the aluminum brazed material. The effects of annealing temperature, atmosphere, and braze process on aluminum alloy composition and thickness were investigated. Results of these studies were correlated with braze performance tests to assist manufacturing operations in the selection of more robust materials and processes.

The aluminum clad/aluminum alloy was subjected to temperature conditions normally used in the brazing process. The surface composition of the clad was measured by XPS prior to heating, after heating at 550 °C, and after heating at 565 °C. The former temperature represents the melting point of the clad, and 565 °C represents the flow temperature of the clad in a brazing process. XPS spectra acquired and the magnesium/aluminum elemental ratios obtained from these spectra at each of the temperatures are given in Fig. 7. The peak at approximately 310 eV is the x-ray induced KLL Auger peak (Ref 5). It is obvious from this peak and the Mg/Al elemental ratios given that the surface composition changes substantially as the temperature is increased to and above the melting point of the clad. Prior to heating, there is very little magnesium as compared to aluminum; however, after the clad flow temperature is reached, the surface is predominantly magnesium relative to aluminum.

The three same materials were cross sectioned and then analyzed by imaging TOF-SIMS to determine the magnesium concentration throughout the clad layer as a function of temperature. Figures 8, 9, and 10 present the Al^+, Si^+, and Mg^+ ion images acquired prior to heating and after 550 and 565 °C, respectively. Definition of the location of the clad layer can be seen by comparing the Al^+ and Si^+ images in each figure. The Si^+ signal should only be seen in this layer, and the Al^+ signal appears more diffuse in the clad layer than in the alloy base. Prior to heating, very little magnesium is observed in the clad layer (Fig. 8c). At the melting point, 550 °C, a somewhat even distribution of low-level magnesium is observed throughout the clad layer as shown in Fig. 9(c). Finally at the clad flow temperature, 565 °C, extensive surface segregation of the magnesium is observed on the clad layer in Fig. 10c. The extensive amount of magnesium observed on the surface of the clad layer after being heated to 565 °C directly correlated with poor brazing performance.

3.3 Example 3—Photodegradation of Multilayer Polymeric Systems

This final example pertains to the TOF-SIMS characterization of model paint systems to determine the effects of photodegradative processes. Example 1 provides a brief discussion of the individual role of each layer in a multilayer automotive paint system. The long term weatherability of these systems is dependent on the ability of each layer to resist weather-induced chemical changes. Conventional means to test the photoresistance of intact modern paint systems have been to observe the actual film integrity during outdoor exposure tests. These tests require up to 5 years to conduct; therefore, accelerated testing procedures have been attempted. However, the accelerated results do not always correlate with

actual in-service performance. In addition, chemistries induced by accelerated testing procedures can be substantially different from those observed after normal exposure (Ref 6). The following example reports the use of imaging TOF-SIMS methodologies in combination with laboratory weathering procedures to determine the relative photooxidation rate of each layer within an intact system.

The laboratory weathering procedure utilized an $^{18}O_2$ rich atmosphere to isotopically label photooxidation products and allow differentiation from polymeric chemistries (Ref 7). This is necessary due to the fact that there is approximately 30% oxygen content in conventional paint systems, and photooxidation products would constitute a small percentage (<1%) of the total oxygen present. Because the TOF-SIMS technique affords
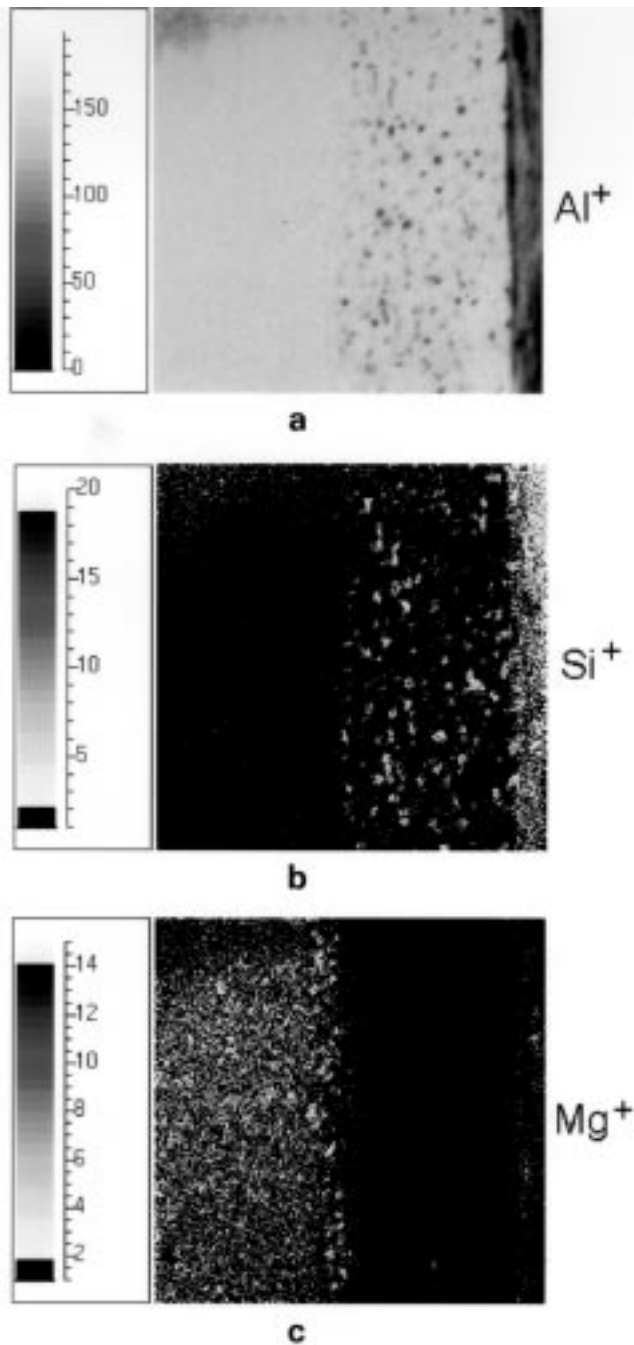

Fig. 8 Time-of-flight secondary ion mass spectrometry ion images of aluminum clad aluminum alloy (a) Al$^+$, (b) Si$^+$, and (c) Mg$^+$ prior to heating
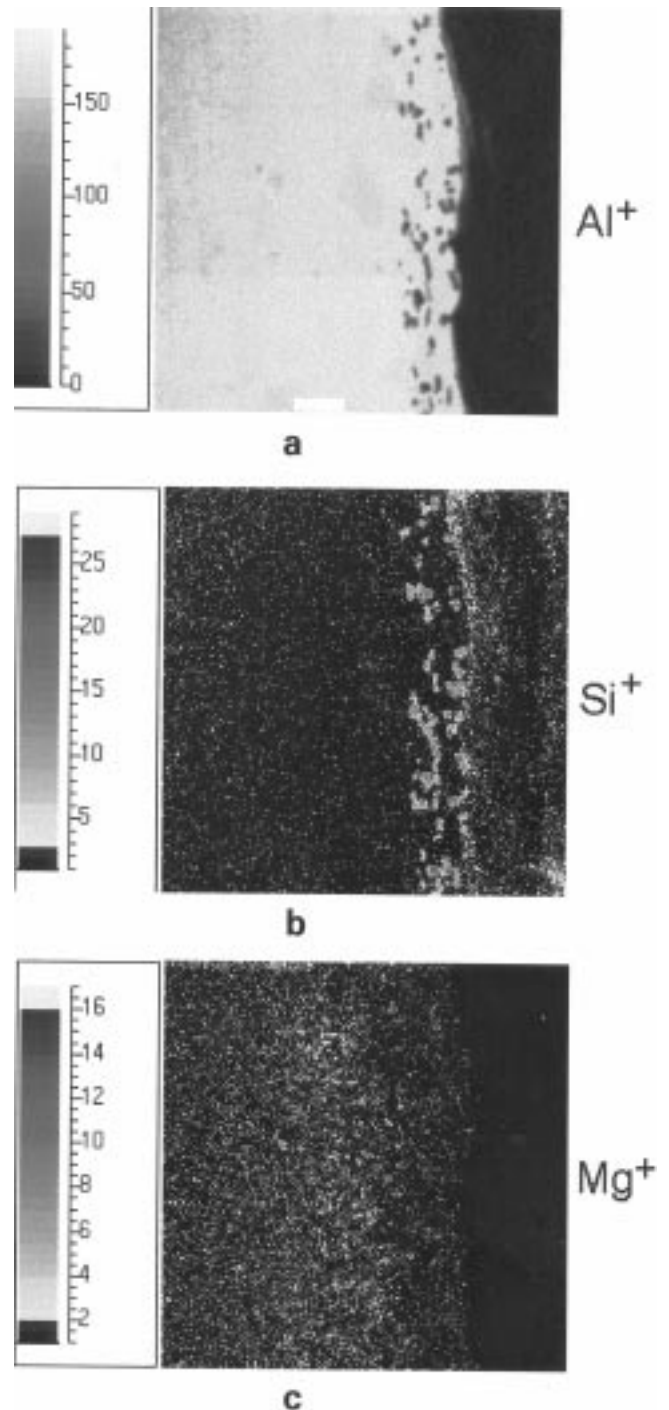

Fig. 9 Time-of-flight secondary ion mass spectrometry ion images of aluminum clad aluminum alloy (a) Al$^+$, (b) Si$^+$, and (c) Mg$^+$ after heating to 550 °C (clad melting point)

isotopic detection, the observance of $^{18}O^-$ beyond its natural abundance is straightforward. Cross-sectional images of the entire system would therefore allow relative comparisons of photooxidation of each layer in the system via comparison of the $^{18}O^-$ intensity observed in each layer. A four-layer model paint system was prepared with coatings of known photooxidation resistance to establish a relationship between coating photooxidation rate and TOF-SIMS $^{18}O^-$ response. A schematic of the model paint system is shown in Fig. 11. The first layer in the model was electrodeposited epoxy/urethane (e-coat) known to rapidly photooxidize. The first layer over the e-coat was an acrylic/melamine clearcoat, Mel-N, known to be relatively resistant to photooxidation.

The next layer was an acrylic/melamine clearcoat, Mel-A, known to photooxidize more rapidly than Mel-N. The final surface layer was an additional layer of Mel-N. The top surface of this model system was then exposed 8 days to ultraviolet radiation using a xenon arc to simulate environmental light exposure. Exposure was undertaken in an atmosphere of $^{18}O_2$ to produce the isotopically labeled photooxidation products. The same experiment was also undertaken in dry air to produce a "control." After exposure, the sample was cleaved to provide a fresh cross-sectional surface.

The TOF-SIMS $^{16}O^-$ and $^{18}O^-$ line scans (not shown) traversing the cross-sectional surface of the control sample of the model paint system (after ultraviolet, UV, exposure in dry air, not enhanced with $^{18}O_2$) were acquired. In both cases ($^{16}O^-$ and $^{18}O^-$), these line scans revealed a relatively uniform distribution of oxygen throughout all the Mel-A and Mel-N layers. The oxygen content observed in polymeric layers can be attributed to a combination of the native oxygen of the original molecular structure and any contribution of photooxidation products induced by the UV experiment. The relatively uniform distribution of oxygen in the Mel-A and Mel-N layers observed in these scans suggests that the results are dominated by the presence of oxygen in the original polymer matrix.

The $^{16}O^-$ TOF-SIMS line scan of the same model paint sample after UV exposure for 8 days in the $^{18}O_2$ atmosphere also reveals a fairly uniform distribution for $^{16}O^-$ response throughout the melamine paint layers and a slight decrease in the e-coat layer (along with the spike from the substrate), as shown in Fig. 12(a). The $^{18}O^-$ line scan in Fig. 12(b), however, reveals substantial differences in the amount of $^{18}O^-$ observed in each layer of the model paint system. Integration of the line scans presented in Fig. 12(b) reveals that the $^{18}O^-$ intensities observed after exposure are approximately 2.3%, 4.8%, and 2.0% of the total $^{16}O^-$ observed for Mel-N, Mel-A, and Mel-N, respectively. The natural isotopic abundance of ^{18}O is 0.2% of the total amount of ^{16}O. Therefore these results indicate that substantial photodegradation has occurred in each of these acrylic melamine layers after exposure. Furthermore Mel-A, the most susceptible of these layers to photooxidation, has photooxidized almost twice as much as each of the Mel-N layers. The Mel-A layer appears to incorporate considerably more $^{18}O^-$ than the overlying Mel-N layer even in the absence of light absorbed by the overlying Mel-N layer. Finally, intense photooxidation is also seen in the e-coat layer.
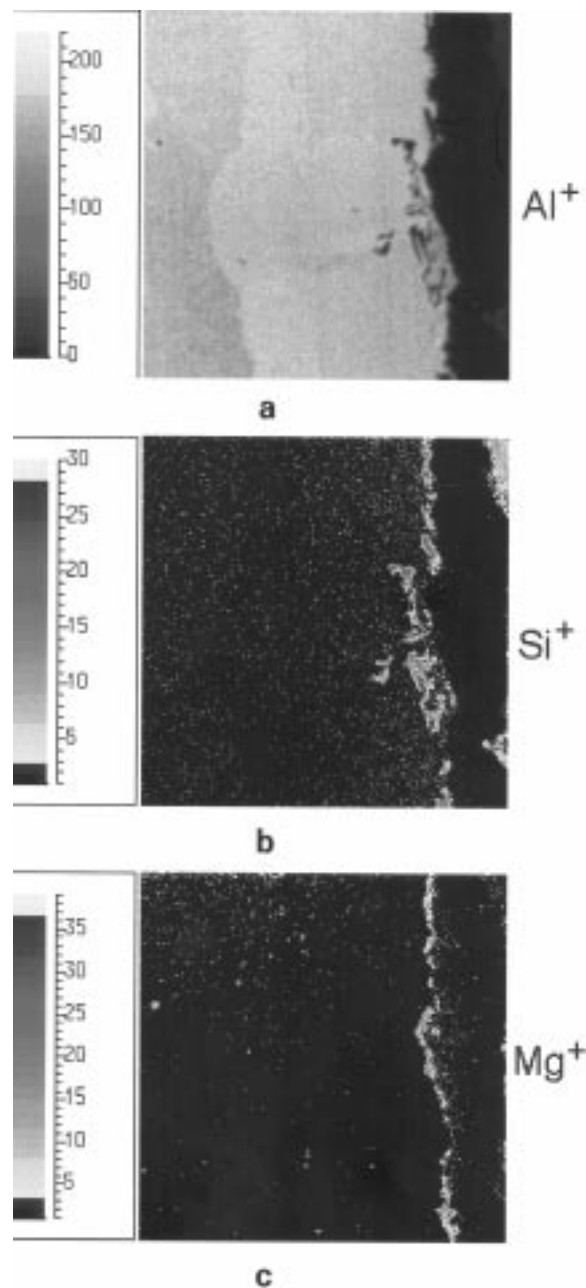

Fig. 10 Time-of-flight secondary ion mass spectrometry ion images of aluminum clad aluminum alloy (a) Al$^+$, (b) Si$^+$, and (c) Mg$^+$ after heating to 565 °C (clad flow temperature)
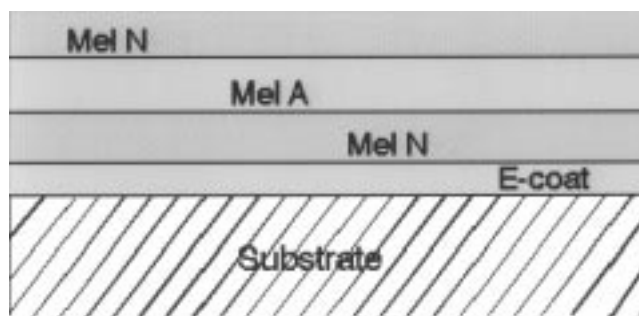

Fig. 11 Schematic of model paint system

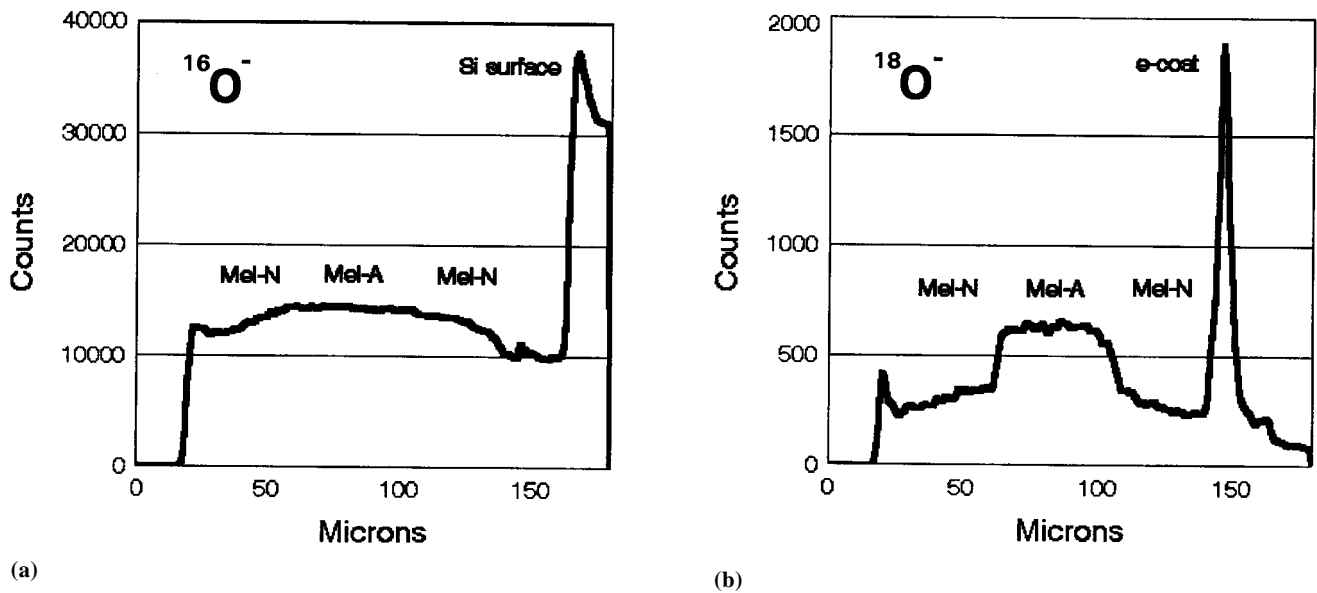**Fig. 12** Time-of-flight secondary ion mass spectrometry linescans of model paint cross section (a) $^{16}O^-$ and (b) $^{18}O^-$

4. Conclusions

The three surface analytical techniques (XPS, SAM, and TOF-SIMS) compliment each other. SAM provided the quantitative and spatial resolution necessary in Example 1, but due to the insulating nature of the paint cross sections in Example 3, TOF-SIMS was utilized. In addition, the isotopic analysis abilities of TOF-SIMS enhanced the molecular information attained in Example 3. The high spatial resolution of the TOF-SIMS combined with the quantitative information attainable by XPS is shown in Example 2.

Acknowledgments

References

1. T.A. Carlson, *Photoelectron and Auger Spectroscopy,* Plenum Press, 1975

2. A.W. Czanderna, *Methods of Surface Analysis,* Elsevier, 1975

3. A. Benninghoven, F.G. Rüdenauer, and H.W. Werner, *Secondary Ion Mass Spectrometry: Basic Concepts, Instrumental Aspects, Applications, and Trends,* John Wiley & Sons, Inc., 1987

4. M. Neay, P. Wilson, and G. Skerl, *J. Coatings Technol.,* Vol 66 (No. 832), 1994, p 27

5. L.E. Davis, N.C. MacDonald, P.W. Palmberg, G.E. Reich, and R.E. Weber, *Handbook of Auger Electron Spectroscopy,* Physical Electronics Industries, Inc., 1978

6. D.R. Bauer, M.C. Paputa Peck, and R.O. Carter, *J. Coatings Technol.,* Vol 59, 1987, p 103

7. J.L. Gerlock, T.J. Prater, S.L. Kaberline, and J.E. deVries, *Polym. Degradation Stab.,* Vol 47, 1995, p 405